Bubble and pattern formation in liquid induced by an electron beam

Joseph M. Grogan[a,†], Nicholas M. Schneider[a], Frances M. Ross[b,+], and Haim H. Bau[a,]*

[a]Department of Mechanical Engineering and Applied Mechanics, the University of Pennsylvania, Philadelphia, PA 19104, USA.

[b]IBM T. J. Watson Research Center, Yorktown Heights, NY 10598, USA.

† Now at Hummingbird Scientific, Lacey, WA 98516, USA.

*bau@seas.upenn.edu

+fmross@us.ibm.com

Abstract: Liquid cell electron microscopy has emerged as a powerful technique for *in situ* studies of nanoscale processes in liquids. An accurate understanding of the interactions between the electron beam and the liquid medium is essential to account for, suppress, and exploit beam effects. We quantify the interactions of high energy electrons with water, finding that radiolysis plays an important role, while heating is typically insignificant. For typical imaging conditions, we find that radiolysis products such as hydrogen and hydrated electrons achieve equilibrium

concentrations within seconds. At sufficiently high dose-rate, the gaseous products form bubbles. We image bubble nucleation, growth, and migration. We develop a simplified reaction-diffusion model for the temporally and spatially varying concentrations of radiolysis species and predict the conditions for bubble formation by H_2. We discuss the conditions under which hydrated electrons cause precipitation of cations from solution, and show that the electron beam can be used to "write" structures directly, such as nanowires and other complex patterns, without the need for a mask.

Liquid cell electron microscopy is a new technique that provides unique capabilities for *in situ* imaging and control of nanoscale phenomena in liquid media with the high resolution of the transmission (TEM) and scanning transmission (STEM) electron microscopes.[1,2] The liquid cell confines a layer of liquid between two membranes and is hermetically sealed from the high vacuum of the microscope. The membranes and liquid are sufficiently thin (tens of nanometers to a few micrometers) to transmit electrons (Figure 1a). Liquid cell (S)TEM provides insights, not readily accessible by other means, into phenomena such as electrochemical processes;[3–6] motion, aggregation, and assembly of nanoparticles;[7–12] nucleation and growth of nanoparticles;[13–18] interactions between particles and interfaces;[19] boiling;[20] macromolecular conformations;[21] and biological processes in cells.[22–24]

During imaging, the electron beam interacts with the sample. Many nanoscale crystallization and growth processes occur only in the beam's presence.[13–18] The beam can be used to charge nanoparticles and affect their motion.[11] Microstructural changes[25] as well as formation and dynamics of bubbles or voids due to the beam have been reported.[20,26–28] Amongst a variety of potential beam effects,[29] radiation chemistry, or interaction of ionizing radiation with the fluid

2

medium, is critically important. Although the existing knowledge of electron beam interactions with solid matter provides useful insights;[30] the effects in liquids are quite different because of the high mobility of species in the liquid. Here we examine two beam-induced nanoscale phenomena, bubble nucleation and growth and beam induced nanostructure formation. We develop a simple reaction-diffusion radiolysis model for the conditions common to electron microscopy, and compare theoretical predictions with experimental observations. We then show that the beam can be used as a "pen" to write nanowires with complex patterns without the need for a mask.

Experiments were performed in our custom-made liquid cell, the nanoaquarium (Figure 1a).[31] In Figure 1b and Supplementary Video 1, we show the formation of nanoscale bubbles during irradiation of an aqueous solution. In this experiment, bubbles form periodically at a serendipitous imperfection on a silicon nitride membrane. The bubble formation occurred while imaging an aqueous solution of gold nanorods (pH ~ 7) with a trace amount of the surfactant cetrimonium bromide (CTAB) with TEM at $300\,\mathrm{keV}$, beam current $I = 1 - 10\,\mathrm{nA}$, and beam radius $a \sim 2\,\mu\mathrm{m}$. Figure 1c depicts the bubbles' radii as a function of time. Note the highly regular periodic nucleation, growth, and detachment of the bubbles.

A second mode of bubble formation is shown in Figure 2a-b and Supplementary Video 2. These larger bubbles are observed after irradiating liquid cells for time intervals ranging from minutes to hours. The bubble in Supplementary Video 2 formed after nearly an hour of $30\,\mathrm{keV}$ STEM imaging of nanoparticle growth in an aqueous solution of $20\,\mathrm{mM}$ $HAuCl_4$ (pH < 2) at a beam current $I = 0.05 - 1.2\,\mathrm{nA}$, beam radius $a \sim 0.5 - 1.5\,\mathrm{nm}$, and raster area of $\sim 1\,\mu\mathrm{m}^2$. Supplementary Video 3 shows another large bubble that formed under similar circumstances. The data of Figure 2c shows that the bubble growth rate increases as the beam current increases.

Large bubbles also form in other solutions: gold nanorods with CTAB (as used in Figure 1) under similar STEM imaging conditions, and various solutions including DI water (pH ~ 7) irradiated in the TEM at $300\,\mathrm{keV}$ with beam current $I = 40 - 50\,\mathrm{nA}$ and beam radius $a \sim 500$ nm.

We consider two possible mechanisms for this beam-induced bubble formation: radiation chemistry (radiolysis) and heating. Both rely on energy transfer from the beam to the sample. Liquid molecules subjected to radiation become excited and ionized, and the resulting radicals, ions, molecular species, and hydrated electrons react chemically to yield byproducts. For water, the primary species generated[32] are e_h (the hydrated electron), H_3O^+, H, OH, H_2, and H_2O_2. Energy transfer that does not exceed the ionization and excitation potentials converts into heat.

To estimate the beam-induced temperature increase, we balance beam-induced heat generation with conductive heat dissipation away from the irradiated region.[7,30] The heat generation is given by

$$q = 10^3 \, \rho \, \Psi \quad (\mathrm{W/m^3}), \tag{1}$$

where

$$\Psi = \frac{10^5 \, S \, I}{\pi \, a^2} \quad (\mathrm{Gy/s}) \tag{2}$$

is the volumetric dose-rate, ρ is the density of the irradiated medium $(\mathrm{g/cm^3})$, I is the beam current $(\mathrm{C/s})$, S is the density-normalized stopping power $(\mathrm{MeV\,cm^2/g\,electron})$, and a is the radius of the beam (m). The factors 10^3 $(\mathrm{cm^3\,J/g\,m^3\,Gy})$ and 10^5 $(\mathrm{m^2\,electron\,Gy\,g/cm^2\,MeV\,C})$ convert units customary to radiation chemistry to SI units. The stopping power S is the average energy loss due to Coulomb interactions per unit path length of a charged particle moving through matter, and it has been tabulated as a function of the

4

incident energy and particle type for various materials.[33] The thermal energy balance leads to a temperature rise of just a few degrees Celsius for typical imaging conditions (see Supporting Information for a detailed derivation), unlikely to produce bubbles by boiling.

In liquid cell experiments, gaseous products of radiolysis are a possible explanation for bubble formation, while the other species produced by radiolysis are strong oxidizing and reducing agents capable of driving or modifying other nanoscale reactions. The amount, or yield, of each species produced (+) or destroyed (−) per 100 eV absorption from ionizing radiation is quantified with an empirical parameter, the G-value (molecules/100 eV).[32] For irradiation of neat water with high energy electrons or positrons, X-rays, γ-rays, and the like, typical values are $G(H_2) = 0.44$ molecules/100 eV and $G(e_h) = 2.7$ molecules/100 eV.[32] The volumetric production rate

$$R_X = \rho\, \Psi\, \frac{G(X)}{e\, N_A} \quad (M/s), \tag{3}$$

of any species X is a function of the rate of energy transfer from the beam and $G(X)$. In the above, e is the electron charge (C/electron), and N_A is the Avogadro number.

Byproduct concentrations do not grow unabated. As is evident from the highly regular bubble formation of Figure 1, under continuous irradiation a steady state is reached. Reverse reactions play a key role, competing with production to yield eventually a steady-state chemical equilibrium with time-invariant product concentrations.[34] To determine the concentration distribution of radiolytic byproducts such as H_2 and e_h, we must account for reverse reactions. We find it convenient to work with a "concentration-dependent effective production rate" Φ_X which accounts for the rate of formation and the reverse reactions of species X. Importantly, the

production rate Φ_X slows down as the concentration C_X approaches the steady state concentration $C_{\text{steady-}X}$. Within the irradiated region

$$\Phi_X = R_X \left(1 - \frac{C_X}{C_{\text{steady-}X}}\right)^{m_X} \qquad \text{if } C_X < C_{\text{steady-}X} \tag{4}$$

$$\Phi_X = 0 \qquad \text{if } C_X \geq C_{\text{steady-X}}.$$

Solutions of the multiple kinetic equations for the radiolytic products indicate that the steady-state concentrations can be correlated with the volumetric dose-rate using a power law[34] of the form

$$C_{\text{steady-}X} = A_X \, \Psi^{r_X}. \tag{5}$$

For example, $A_{H_2} \sim 9.3 \times 10^{-7} \text{ M (s/Gy)}^{-r_{H_2}}$, $r_{H_2} \sim 0.44$, $A_{e_h} \sim 1.2 \times 10^{-11} \text{ M (s/Gy)}^{-r_{e_h}}$, and $r_{e_h} \sim 0.59$ for deaerated water at pH 6.[34] By matching the predictions of equation (4) with available experimental data, we find that $m_{H_2} \sim 2$ provides a good fit between our theoretical predictions and published experimental data.[34]

Outside the irradiated region, the rate of extinction of reactive species is modeled with an expression of the form: $-C_X/\tau_X$, where τ_X is the relaxation time. For example, for hydrated electrons $\tau_{e_h} \sim 50$ μs, while for the relatively non-reactive hydrogen $\tau_{H_2} \rightarrow \infty$.[35]

Equations (4) and (5) give us a simple framework with which to predict the concentration distributions of radiolysis byproducts as functions of time, position, irradiation dose rate, and electron beam position and size, using them as the source terms in reaction-diffusion equations. We carried out finite element calculations to predict the concentration distribution of two species, H_2 and e_h, using equation (4) as the production term in a two-dimensional reaction-diffusion equation within the geometry of the liquid cell (Figure 3a and Supporting Information). Figure 3b depicts the H_2 concentration C_{H_2} at the center of the beam as a function of time when

the beam current is 0.1, 1, and 10 nA. The concentration initially increases rapidly upon irradiation and then the concentration-dependent effective production rate decays. A key result is that it only takes a few seconds of irradiation for C_{H_2} to asymptotically approach its dose-rate dependent steady-state value $C_{steady\text{-}H_2}$. This is shorter than the timescale of most *in situ* experiments. Figure 3c depicts C_{H_2} at the center of the beam as a function of beam current at various times. The dashed lines in Figure 3b and c correspond to the saturation concentration at atmospheric pressure. Figure 3d depicts the spatial distribution of the normalized concentrations of H_2 and e_h at various times.

We can now relate these estimates of H_2 concentration to the observations of bubbles in Figures 1 and 2. To form a bubble from gas dissolved in liquid, the dissolved gas concentration must significantly exceed the saturation concentration (C_{sat}), which depends on the pressure of the system. Using Henry's Law[36] for H_2 in water, we estimate $C_{sat}(100\text{ kPa}) \sim 0.77\text{ mM}$ and $C_{sat}(400\text{ kPa}) \sim 3.15\text{ mM}$ (reasonable values for the pressure in a liquid-cell). Homogeneous nucleation requires a large supersaturation, experimentally measured to be $C_{homogeneous} \sim 190\text{ mM}$ for H_2 at $100 - 400\text{ kPa}$.[37] Heterogeneous nucleation can occur stochastically at any concentration between C_{sat} and $C_{homogeneous}$. Indeed, for the conditions of our experiments, Figure 3 predicts that $C_{sat} < C_{H_2} < C_{homogeneous}$. Thus, supersaturated radiolytic H_2 is likely the main contributor to bubble nucleation during liquid cell (S)TEM imaging of aqueous solutions. O_2 is predicted to form as a secondary byproduct with steady-state concentration that can approach that of H_2.[34,38] With a strong dependence on solution composition, a longer timescale compared to the primary byproducts, and an aqueous solubility that is greater than that of H_2, O_2 is less likely to be the cause of bubble nucleation.[36] However, once a bubble is formed, O_2 will contribute to its growth. The important prediction that

continuous irradiation leads to a steady-state H_2 concentration is validated by the periodic, regular nanoscale bubble formation shown in Figure 1 and Supplementary Video 1. The observations indicate that the system is, indeed, in a state of equilibrium, with rates of nucleation and growth that do not vary significantly with time.

The model also explains the role of irradiation time. When $C_{\text{steady-H}_2} > C_{\text{sat}}$, supersaturated H_2 spreads by diffusion from the beam region to the rest of the liquid cell (Figure 3d). With time, this increases the probability of heterogeneous nucleation and provides more H_2 molecules to feed a bubble once formed. Bubble-free imaging requires conditions such that $C_{\text{steady-H}_2}$ does not greatly exceed C_{sat} (dashed lines in Figure 3b and c). Had we not modified equation (3) to consider the concentration-dependent effective production rate, the model would have predicted $C_{H_2} \sim 264$ mM ($> C_{\text{homogeneous}}$) after only 60 seconds for 300 keV electrons with $a = 500$ nm and $I = 40$ nA. The fact that we, and others,[16] are able to image at a high dose-rate for moderate time intervals without observing bubbles suggests that the effective H_2 production rate is indeed reduced as radiolytic byproducts accumulate.

Our model for the temporal and spatial variation of radiolytic byproducts suggests an important application of the electron beam to form nanoscale structures controllably. Highly reactive radiolysis products such as the hydrated electron have short diffusion distances and are therefore present at high concentrations only in the irradiated region (Figure 3d). Thus, reactions mediated by hydrated electrons can, in principle, be localized to the irradiated (beam) area. An interesting application is shown in Figure 4. The reduction of Au ions to neutral Au is known to be mediated by hydrated electrons.[39] Scanning a focused electron beam over a region containing a thin film of $HAuCl_4$ solution resulted in the precipitation of gold and the formation of gold nanowires, making up nanoscale letters, in this case the names of the authors' institutions (Figure

4a). The structures appeared robust. Bubble motion tossed the features about, indicating that they could be detached by surface tension forces without damage (Figure 4b). This liquid-phase electron beam induced deposition is an intriguing technique for generating micro- and nanowires with controlled sizes and patterns without the use of a mask and has been explored in this and other materials.[40,41]

We now briefly discuss the limitations of the model. The data used in developing equations (4) and (5) were measured for low dose-rate irradiation (< 1000 Gy/s). However, the dose-rates in liquid cell (S)TEM experiments are often orders of magnitude higher than those considered by radiation chemists. For example, a 300 keV electron beam with $a = 500$ nm and $I = 1$ nA in water corresponds to 3×10^8 Gy/s. It is therefore necessary to consider the consequences of a high dose-rate irradiation. Increasing the dose-rate increases the likelihood that radical byproducts will interact to yield molecular species, which for neat water include H_2, H_2O_2, and recombined H_2O.[38] We estimate that under typical imaging conditions, these non-linear effects are unlikely in the TEM but possible in the STEM (Supporting Information), potentially changing concentrations by large amounts.

Our model also ignores the effect of solution composition (*e.g.*, additives and pH). It is known that $C_{\text{steady-H}_2}$ depends strongly – changing by orders of magnitude – on the degree of aeration and pH of the solution.[34] Even at low concentration, a solute (*e.g.*, N_2 and O_2 due to aeration) may react with radiolysis byproducts to affect the chemistry of the system. At a high concentration, a solute may fundamentally alter the production rate of radiolysis byproducts by scavenging radicals. Since all the species in a system are interrelated *via* coupled reactions, predictive calculations of transient and steady-state behavior require analysis of the complete chemical kinetics. Future analysis will provide insight into whether, or how, these dependencies

on solution composition might apply at the high dose-rates of liquid-cell (S)TEM. We have assumed that equations (4) and (5) can be applied to radiolysis in both TEM and STEM for the solutions we have discussed above.

In summary, liquid cell electron microscopy is a powerful *in situ* technique that provides a unique insight into processes in liquid media. The electron beam affects the chemistry and behavior of the solution under observation, however. Our experimental data indicates that the concentrations of the radiolysis products reach equilibrium when subjected to the high dose radiation common in electron microscopy. We have imaged nucleation and measured the growth rate of nanoscale bubbles and microscale "explosive" bubbles. We have also developed a simple quantitative model for the concentrations of radiolysis products, such as H_2, as functions of space and time. The model predictions are consistent with our experimental observations. A central feature of this model is the concentration-dependent effective production rate, which allows the concentrations of radiolysis products to reach a steady state chemical equilibrium. The key predictions of the model are that this steady-state is reached rapidly, within seconds; and that when bubbles are observed, the predicted concentrations are consistent with those required to nucleate bubbles. For example, H_2 can exceed its saturation concentration within seconds to minutes of imaging with only moderate beam current. The temporally and spatially varying concentrations of other radiolysis byproducts can be calculated in a manner analogous to what we have described for H_2. We have shown that one species, the hydrated electron, will be strongly confined to the irradiated area, making it possible to write nanoscale features such as letters from gold and other metallic solutions. Other highly reactive radical and ionic byproducts should follow trends similar to that of e_h.

Radiolysis is of key importance in nuclear science, medical imaging and therapeutics, food preservation, and other manufacturing processes. Knowledge acquired in these fields is applicable to liquid cell electron microscopy. Conversely, the liquid cell provides a useful tool to study radiation effects. We believe that the fundamental beam-sample interactions discussed here are relevant to chemical reaction processes that occur during liquid cell (S)TEM in media other than water, and environmental scanning electron microscopy (ESEM) where water vapor is present and the sample may be fully hydrated or enveloped with a water layer. Radiation chemistry must be considered in all liquid cell experiments. For example, the increase in the ion concentration in an irradiated colloidal suspension may reduce the thickness of the Debye screening length and induce aggregation, and hydrated electrons may neutralize cations and allow precipitation. Even if there are no bubbles, one cannot dismiss the invisible beam effects; highly reactive species are continuously produced during beam irradiation. A detailed understanding of radiation chemistry is essential to predict, account for, mitigate, and harness beam effects in the rapidly growing field of liquid cell electron microscopy.
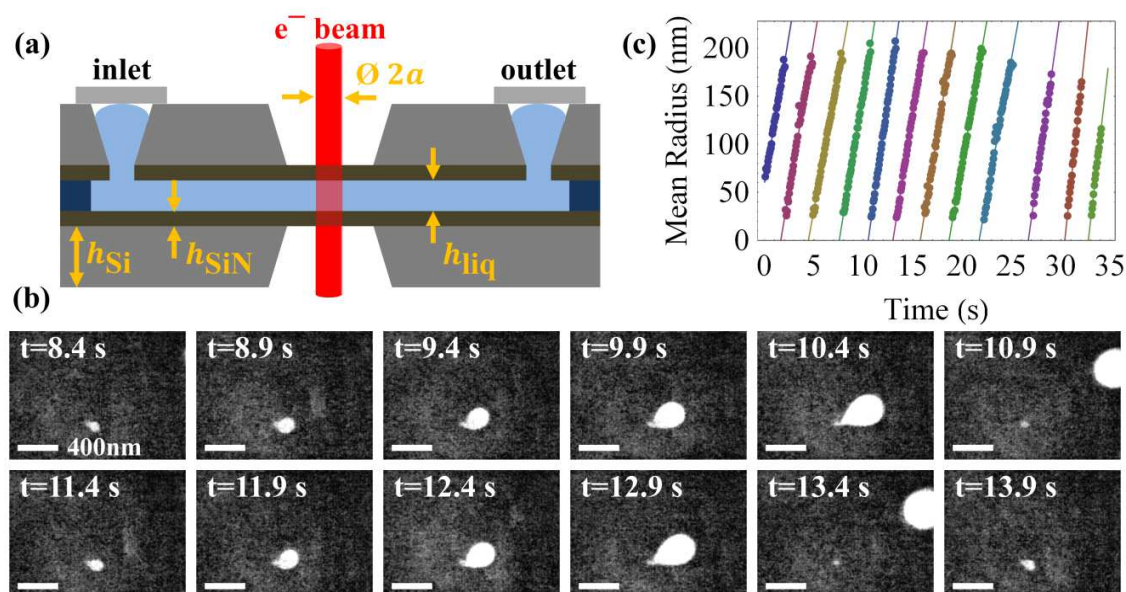
Figure 1. A schematic of a liquid cell and observations of small bubbles. (a) A schematic illustration of a sealed liquid cell cross-section, not drawn to scale. $h_{Si} = 300\ \mu m$. $h_{SiN} = 50\ nm$. h_{liq} is nominally $100 - 300\ nm$, though membrane bowing can result in h_{liq} of a few μm.[31] (b) Frames from a video sequence (Supplementary Video 1) of heterogeneous bubble nucleation, growth, and migration during TEM imaging (300 keV, $I < 1\ nA$, beam radius $a \sim 2\ \mu m$). A bubble nucleates on the membrane, grows, and detaches. Another bubble nucleates at the same spot and the process repeats. Observed bubble radii ranged from 20 to 200 nm. (c) Mean bubble radius as a function of time (example 1 of Supplementary Video 1). Colored circles represent experimental data and lines are linear fits. On average, bubbles grew at a nearly constant rate of $\dot{b} \sim 70\ nm/s$, nucleated at a frequency $f \sim 0.3\ Hz$, and reached a maximum radius $\bar{b}_{max} \sim 190\ nm$ in 3.1 seconds before detaching and migrating out of the field of view.

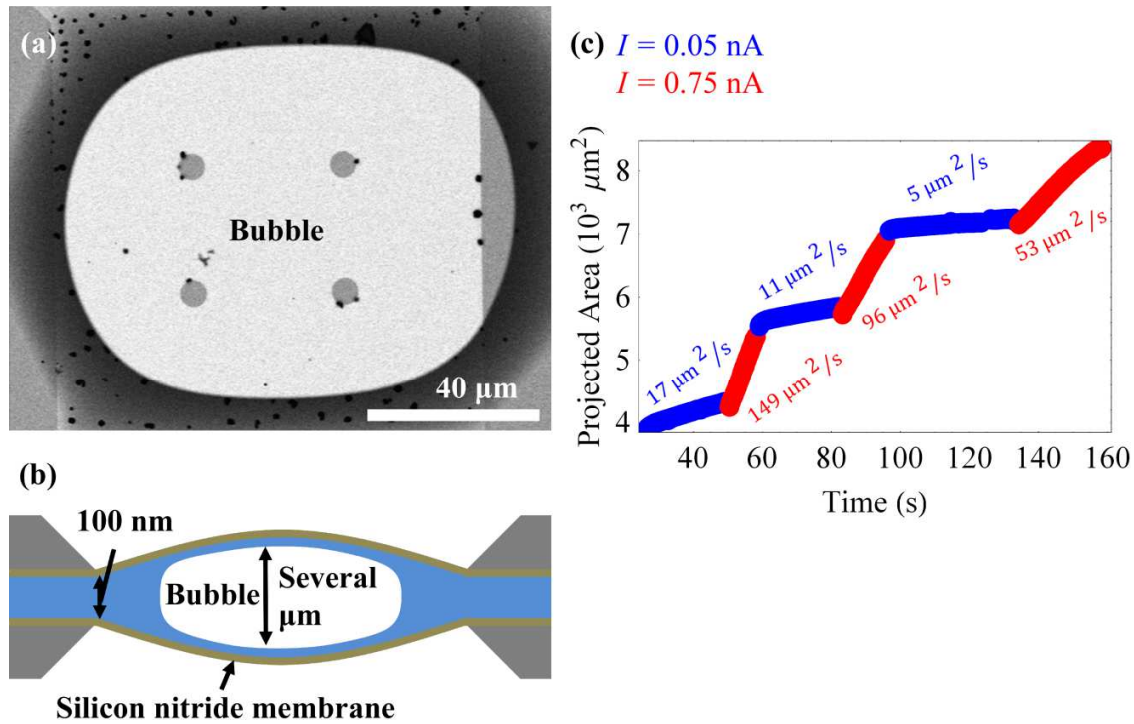**Figure 2.** Observations of "explosive" bubbles in 20 mM $HAuCl_4$ (pH < 2) by STEM. (a) A large bubble occupying most of the membrane window. Liquid is pushed to the periphery (Supplementary Video 2). Prior to the formation of this bubble, various parts of the window were irradiated for periods lasting from tens of seconds to a few minutes at each location. The small black dots are gold nanoparticles nucleated by the beam during this time. (30 keV, $I = 0.05 - 1.2$ nA, beam radius $a \sim 0.5 - 1.5$ nm, raster area $\sim 1\ \mu m^2$). The four grey circles are SiO_2 pillars that were designed to hold the top and bottom membranes together to reduce membrane deflection. (b) A schematic of the liquid cell cross-section with a large bubble in the imaging window. A thin film of liquid remains on the membranes, as shown by continued nucleation of nanoparticles in the illuminated region. Subsequent inspection with a light microscope revealed that the membranes were bowed out by several μm. (c) The projected bubble area as a function of time (Supplementary Video 3). The beam current alternated between 0.05 nA and 0.75 nA, which affected the bubble growth rate. The bubble's approximate area growth rate ($\mu m^2/s$) is indicated in the plot. The growth rate decreases as the bubble displaces liquid and fills more of the imaging window.
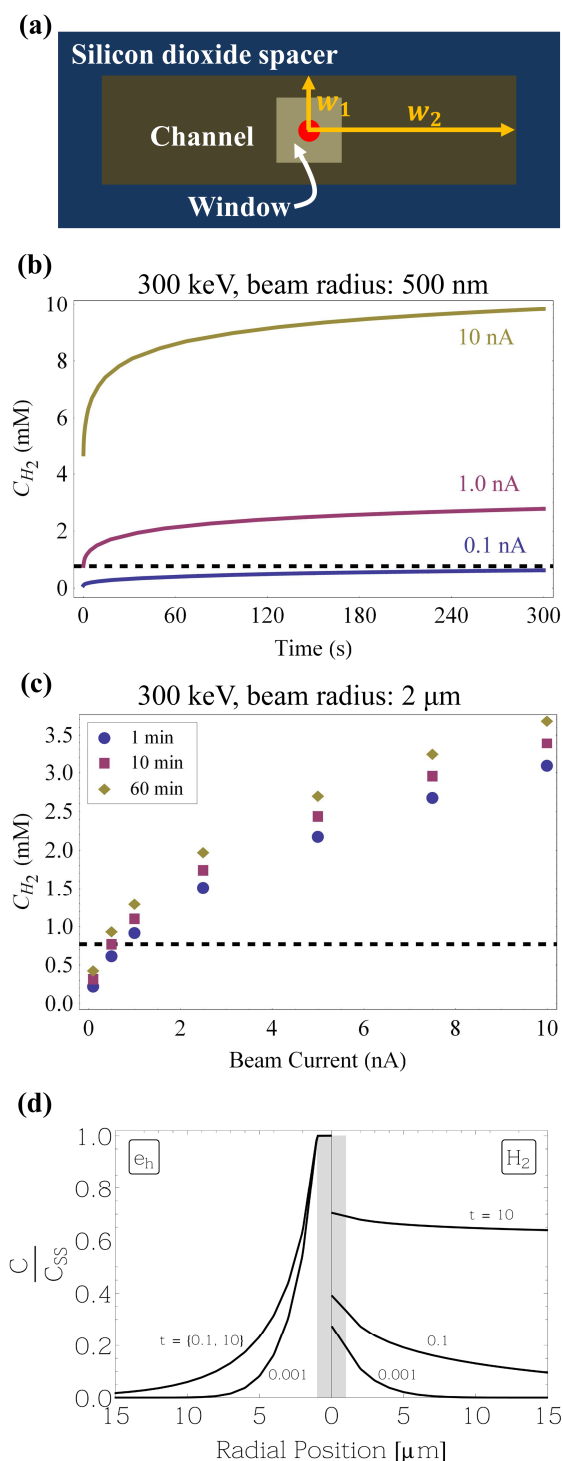
(a)

(b)

(c)

(d)

Figure 3. Modeling the concentration of radiolysis products in the liquid cell. (a) A schematic illustration of the liquid cell geometry used in the simulation. Impermeable boundaries are specified at $2w_1 = 100$ µm and $2w_2 = 8$ mm to reflect the dimensions of our device. The red

14

dot, representing the beam, is located at the center of the imaging window. Placing the beam off-center does not change the results substantially. The predicted H_2 concentration at the center of the beam or raster area is depicted as a function of irradiation time for various beam currents (b) and as a function of beam current for various times (c). The black dashed line corresponds to the saturation concentration $C_{sat}(100 \text{ kPa}) = 0.77$ mM. The region under the dashed line provides a conservative estimate of the range of currents and time intervals for bubble-free operation. (d) The predicted concentration $C_X/C_{steady\text{-}X}$ of H_2 (right) and e_h (left) in and around the irradiated area of radius 1 µm (grey stripe) as a function of distance from the beam center at various times (seconds).
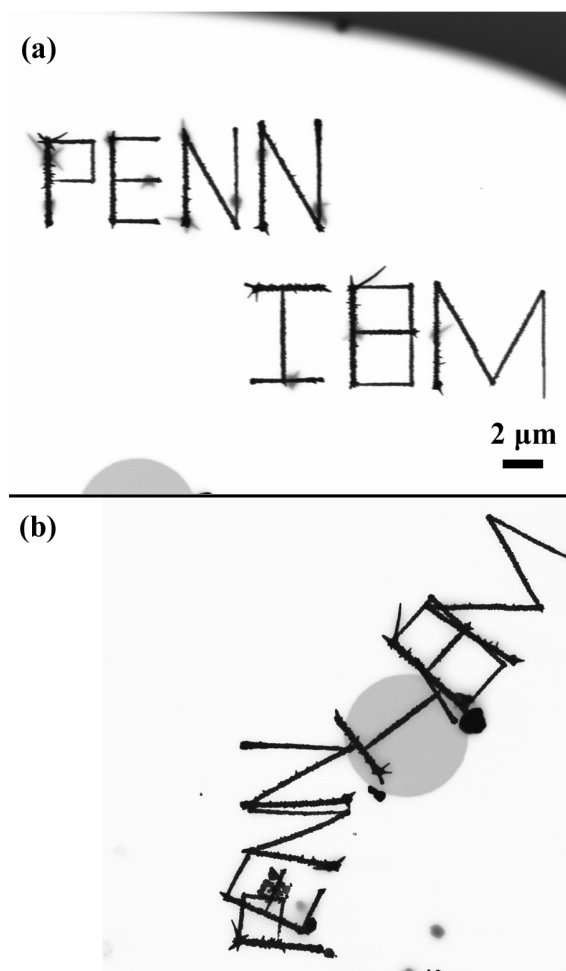
Figure 4. Beam-induced precipitation of gold from 20 mM HAuCl$_4$ solution. (a) By controlling the dose-rate and exposed area in the liquid cell, precipitation of Au at the liquid/SiN interface was controlled in order to "write" nano-letters. The letters were written following the generation of the large bubble in Supplementary Video 2 (30 KeV STEM with 20 mM HAuCl$_4$), after which a thin liquid layer remained wetting the membrane (as in Figure 2). (b) Following the collapse and reformation of a large bubble, the beam-induced letters were dislodged from the membrane surface, but remain intact.

ASSOCIATED CONTENT

"Video observations and analysis of bubble formation and growth," "Estimates of Beam-Induced Heating," "Water radiolysis by electrons and other high energy species," "Non-linear dose rate effects in STEM and TEM," and "Reaction-Diffusion Model & Finite Element Modeling for H_2"are supplied as Supporting Information. This material is available free of charge via the Internet at http://pubs.acs.org.

Competing Financial Interests

F.M.R., H.H.B., and N.M.S. declare no competing financial interests. J.M.G. now works for

Hummingbird Scientific, a developer of sample holders for electron and ion microscopy, which

include holders for liquid cell (S)TEM. Hummingbird Scientific has no relationship to the

reported work and the instruments used in the experiments are not products of Hummingbird

Scientific.

REFERENCES

1. Jonge, N. de; Ross, F. M. Electron Microscopy of Specimens in Liquid. *Nat Nano* **2011**, *6*, 695–704.
2. Grogan, J. M.; Schneider, N. M.; Ross, F. M.; Bau, H. H. The Nanoaquarium: A New Paradigm in Electron Microscopy. *Journal of the Indian Institute of Science* **2012**, *92*, 295–308.
3. Williamson, M. J.; Tromp, R. M.; Vereecken, P. M.; Hull, R.; Ross, F. M. Dynamic Microscopy of Nanoscale Cluster Growth at the Solid-liquid Interface. *Nat Mater* **2003**, *2*, 532–536.
4. Radisic, A.; Vereecken, P. M.; Hannon, J. B.; Searson, P. C.; Ross, F. M. Quantifying Electrochemical Nucleation and Growth of Nanoscale Clusters Using Real-Time Kinetic Data. *Nano Letters* **2006**, *6*, 238–242.
5. Radisic, A.; Vereecken, P. M.; Searson, P. C.; Ross, F. M. The Morphology and Nucleation Kinetics of Copper Islands During Electrodeposition. *Surface Science* **2006**, *600*, 1817–1826.
6. White, E. R.; Singer, S. B.; Augustyn, V.; Hubbard, W. A.; Mecklenburg, M.; Dunn, B.; Regan, B. C. In Situ Transmission Electron Microscopy of Lead Dendrites and Lead Ions in Aqueous Solution. *ACS Nano* **2012**, *6*, 6308–6317.
7. Zheng, H.; Claridge, S. A.; Minor, A. M.; Alivisatos, A. P.; Dahmen, U. Nanocrystal Diffusion in a Liquid Thin Film Observed by in Situ Transmission Electron Microscopy. *Nano Letters* **2009**, *9*, 2460–2465.
8. Ring, E. A.; Jonge, N. de Microfluidic System for Transmission Electron Microscopy. *Microscopy and Microanalysis* **2010**, 1–8.
9. Grogan, J. M.; Rotkina, L.; Bau, H. H. In Situ Liquid-cell Electron Microscopy of Colloid Aggregation and Growth Dynamics. *Phys. Rev. E* **2011**, *83*.
10. Li, D.; Nielsen, M. H.; Lee, J. R. I.; Frandsen, C.; Banfield, J. F.; Yoreo, J. J. De Direction-Specific Interactions Control Crystal Growth by Oriented Attachment. *Science* **2012**, *336*, 1014–1018.
11. White, E. R.; Mecklenburg, M.; Shevitski, B.; Singer, S. B.; Regan, B. C. Charged Nanoparticle Dynamics in Water Induced by Scanning Transmission Electron Microscopy. *Langmuir* **2012**, *28*, 3695–3698.

12. Park, J.; Zheng, H.; Lee, W. C.; Geissler, P. L.; Rabani, E.; Alivisatos, A. P. Direct Observation of Nanoparticle Superlattice Formation by Using Liquid Cell Transmission Electron Microscopy. *ACS Nano* **2012**, *6*, 2078–2085.
13. Evans, J. E.; Jungjohann, K. L.; Browning, N. D.; Arslan, I. Controlled Growth of Nanoparticles from Solution with In Situ Liquid Transmission Electron Microscopy. *Nano Lett.* **2011**, *11*, 2809–2813.
14. Zheng, H.; Smith, R. K.; Jun, Y.; Kisielowski, C.; Dahmen, U.; Alivisatos, A. P. Observation of Single Colloidal Platinum Nanocrystal Growth Trajectories. *Science* **2009**, *324*, 1309–1312.
15. Noh, K. W.; Liu, Y.; Sun, L.; Dillon, S. J. Challenges Associated with In-situ TEM in Environmental Systems: The Case of Silver in Aqueous Solutions. *Ultramicroscopy* **2012**, *116*, 34–38.
16. Liao, H.-G.; Cui, L.; Whitelam, S.; Zheng, H. Real-Time Imaging of Pt3Fe Nanorod Growth in Solution. *Science* **2012**, *336*, 1011–1014.
17. Yuk, J. M.; Park, J.; Ercius, P.; Kim, K.; Hellebusch, D. J.; Crommie, M. F.; Lee, J. Y.; Zettl, A.; Alivisatos, A. P. High-Resolution EM of Colloidal Nanocrystal Growth Using Graphene Liquid Cells. *Science* **2012**, *336*, 61–64.
18. Woehl, T. J.; Evans, J. E.; Arslan, I.; Ristenpart, W. D.; Browning, N. D. Direct in Situ Determination of the Mechanisms Controlling Nanoparticle Nucleation and Growth. *ACS Nano* **2012**, *6*, 8599–8610.
19. Grogan, J. M.; Bau, H. H. Real Time Electron Microscope Imaging of Nanoparticle Motion Induced by a Moving Contact Line. *arXiv.org* **2011**.
20. White, E. R.; Mecklenburg, M.; Singer, S. B.; Aloni, S.; Regan, B. C. Imaging Nanobubbles in Water with Scanning Transmission Electron Microscopy. *Applied Physics Express* **2011**, *4*, 055201.
21. Mirsaidov, U. M.; Zheng, H.; Casana, Y.; Matsudaira, P. Imaging Protein Structure in Water at 2.7 Nm Resolution by Transmission Electron Microscopy. *Biophysical Journal* **2012**, *102*, L15–L17.
22. Jonge, N. de; Peckys, D. B.; Kremers, G. J.; Piston, D. W. Electron Microscopy of Whole Cells in Liquid with Nanometer Resolution. *Proceedings of the National Academy of Sciences* **2009**, *106*, 2159–2164.
23. Peckys, D. B.; Veith, G. M.; Joy, D. C.; Jonge, N. de Nanoscale Imaging of Whole Cells Using a Liquid Enclosure and a Scanning Transmission Electron Microscope. *PLoS ONE* **2009**, *4*, e8214.
24. Dukes, M. J.; Peckys, D. B.; Jonge, N. de Correlative Fluorescence Microscopy and Scanning Transmission Electron Microscopy of Quantum-Dot-Labeled Proteins in Whole Cells in Liquid. *ACS Nano* **2010**, *4*, 4110–4116.
25. Stoll, J. D.; Kolmakov, A. Electron Transparent Graphene Windows for Environmental Scanning Electron Microscopy in Liquids and Dense Gases. *Nanotechnology* **2012**, *23*.
26. Klein, K. L.; Anderson, I. M.; Jonge, N. De Transmission Electron Microscopy with a Liquid Flow Cell. *Journal of Microscopy* **2011**, *242*, 117–123.
27. Mirsaidov, U.; Ohl, C.-D.; Matsudaira, P. A Direct Observation of Nanometer-size Void Dynamics in an Ultra-thin Water Film. *Soft Matter* **2012**, *8*, 7108.
28. Huang, T.-W.; Liu, S.-Y.; Chuang, Y.-J.; Hsieh, H.-Y.; Tsai, C.-Y.; Wu, W.-J.; Tsai, C.-T.; Mirsaidov, U.; Matsudaira, P.; Chang, C.-S.; *et al.* Dynamics of Hydrogen Nanobubbles in KLH Protein Solution Studied with in Situ wet-TEM. *Soft Matter* **2013**, *9*, 8856.
29. Woehl, T. J.; Jungjohann, K. L.; Evans, J. E.; Arslan, I.; Ristenpart, W. D.; Browning, N. D. Experimental Procedures to Mitigate Electron Beam Induced Artifacts During in Situ Fluid Imaging of Nanomaterials. *Ultramicroscopy* **2012**.
30. Egerton, R. F.; Li, P.; Malac, M. Radiation Damage in the TEM and SEM. *Micron* **2004**, *35*, 339–409.
31. Grogan, J. M.; Bau, H. H. The Nanoaquarium: A Platform for In Situ Transmission Electron Microscopy in Liquid Media. *Journal of Microelectromechanical Systems* **2010**, *19*, 885–894.
32. Mozumder, A. *Fundamentals of Radiation Chemistry*; Academic Press, 1999.

33. Berger, M. J.; Coursey, J. S.; Zucker, M. A.; Chang, J. NIST Stopping-Power and Range Tables: Electrons, Protons, Helium Ions http://www.nist.gov/pml/data/star/index.cfm/ (accessed Aug 14, 2012).

34. Joseph, J. M.; Seon Choi, B.; Yakabuskie, P.; Clara Wren, J. A Combined Experimental and Model Analysis on the Effect of pH and O2(aq) on Γ-radiolytically Produced H2 and H2O2. *Radiation Physics and Chemistry* **2008**, *77*, 1009–1020.

35. Siefermann, K. R.; Liu, Y.; Lugovoy, E.; Link, O.; Faubel, M.; Buck, U.; Winter, B.; Abel, B. Binding Energies, Lifetimes and Implications of Bulk and Interface Solvated Electrons in Water. *Nat Chem* **2010**, *2*, 274–279.

36. Cengel, Y. A.; Boles, M. A. *Thermodynamics: An Engineering Approach*; 3rd ed.; WCB/McGraw-Hill, 1998.

37. Finkelstein, Y.; Tamir, A. Formation of Gas Bubbles in Supersaturated Solutions of Gases in Water. *AIChE journal* **1985**, *31*, 1409–1419.

38. Pastina, B.; LaVerne, J. A. Effect of Molecular Hydrogen on Hydrogen Peroxide in Water Radiolysis. *The Journal of Physical Chemistry A* **2001**, *105*, 9316–9322.

39. Chernyak, A. S.; Zhigunov, V. A.; Shepot'ko, M. L.; Smirnov, G. I.; Dolin, P. I.; Bobrova, A. S.; Khikin, G. I. Precipitation of Gold and Silver from Cyanide Solutions by Hydrated Electrons Generated by Ionizing Radiation. *Journal of Applied Chemistry of the USSR* **1981**, *54*, 1024–1026.

40. Donev, E. U.; Hastings, J. T. Electron-Beam-Induced Deposition of Platinum from a Liquid Precursor. *Nano Letters* **2009**, *9*, 2715–2718.

41. Schardein, G.; Donev, E. U.; Hastings, J. T. Electron-beam-induced Deposition of Gold from Aqueous Solutions. *Nanotechnology* **2011**, *22*, 015301.